npj | 2D Materials and Applications

www.nature.com/npj2dmaterials

ARTICLE OPEN

Check for updates

Titanium disulfide as Schottky/ohmic contact for monolayer molybdenum disulfide

Junsen Gao[1] and Manisha Gupta[1]✉

2D semiconductors like Molybdenum disulfide (MoS_2) still have issues in forming good metal electrode (Schottky and Ohmic) especially for mono layer (ML) to few layers thick due to strain and metallization issues. Here, we explore a 2D semi-metal, titanium disulfide (TiS_2), for making different types of contacts with ML MoS_2 using density functional theory (DFT). It is observed that ML TiS_2 induces ML MoS_2 to become p-type with a doping density of 3.85×10^{17} cm^{-3} which becomes larger with thicker TiS_2. Thus, TiS_2 can thus be utilized as a variable contact material ohmic if the MoS_2 is p-type and as Schottky if the MoS_2 is n-type with a Schottky barrier height ranging from 0.3 to 1.35 eV. One of the important results from the study is that compared to a traditional metal–MoS_2 in a TiS_2–MoS_2 contact the bandgap is preserved where in contrast, a traditional metal contact metalizes the monolayer MoS_2 and fill its bandgap with states. Hence, a clear path forward to make pristine contacts is to use 2D semi-metals in conjunction with 2D semiconductors.

npj 2D Materials and Applications (2020)4:26 ; https://doi.org/10.1038/s41699-020-00161-5

INTRODUCTION

In recent years, molybdenum disulfide (MoS_2), one of the transition metal dichalcogenide monolayers (TMDC), has attracted significant attention and has been explored for a variety of applications in a vast range of fields[1–3]. Inter-layer van der Waals bonding of MoS_2 allows one to obtain monolayer (ML) thickness[4]. Due to its 2D nature, the ML MoS_2 shows planar structure without the presence of the dangling bonds. This gives ML MoS_2 perfect surface smoothness and helps reduce the surface trap states[5]. Compared to other 2D materials, MoS_2 has a non-zero layer-dependent bandgap, which is 1.2 eV indirect bandgap[6] for bulk MoS_2 and 1.8 eV direct bandgap[7] for ML MoS_2. This unique property enables ML or multilayer MoS_2 to act as a semiconductor and thus broadens the application of MoS_2 in the field of electronics and photonics. MoS_2 also has other merits like good flexibility[8], adequate mobility[9], and availability of large-scale thin films (synthesis)[10]. For these reasons, MoS_2 is fast becoming a promising candidate for the 2D semiconducting channel of the next-generation field effect transistors (FET). Although many MoS_2 FET have been reported[11–13], obtaining a good contact for MoS_2 FET is still an important issue. To find both good ohmic and Schottky contacts, extensive research has been conducted to investigate metal–(ML) MoS_2 contacts[14–18] via both computational and experimental work. However, it is observed that the covalent bonds forming between the metal and MoS_2 introduce defects and metallization effect the MoS_2 structure[14,18], which can be seen in Fig. 1a. After creating a contact, the defects generated lower charge mobility[18]. To overcome this issue, some groups have utilized encapsulation technique, the MoS_2 mobility can be preserved by using hexagonal boron nitride (h-BN) nano sheets to enclose the MoS_2 sheet[19,20]. This encapsulation technique though increases the fabrication complexity of the devices which add difficulty for large-scale manufacturing.

To overcome the existing issues of the metal–MoS_2 contact, the concept of van der Waals contact based on 2D metals and semimetals has been studied earlier[21]. In recent years, many MoS_2 devices integrated with 2D contacts have been fabricated[22–24]. Compared with traditional metal contacts, these contacts show higher mobility, smaller structural changes in MoS_2 and smaller metallization is added to MoS_2 along with higher flexibility. The h-BN encapsulation can also be used for these contacts with its deposition by chemical vapor deposition (CVD) or exfoliation to further increase the device mobility[24,25]. Thus, utilizing 2D materials as a electrode material improves the scalability of the devices. It has been shown that smoothness, absence of dangling bonds, and the ultra-thin layer of the 2D contact enables shorter channel devices in 2D MoS_2 FET[25]. Obtaining good and reliable ohmic and Schottky contacts for MoS_2 will speed up the development of high-performance 2D heterostructure devices.

It is thus essential to explore and understand 2D materials suitable for electrode formation with MoS_2. There are quite a few 2D metallic materials and we consider titanium disulfide (TiS_2 for the electrode here). TiS_2 is also a member of TMDC family, but there is a small overlap between the conduction band and valence band of TiS_2[26]. Some references have claimed that TiS_2 has a narrow bandgap of 0.2 eV[27] exhibiting semi-metallic properties. As a semi-metallic material, TiS_2 has already been employed as electrode material of lithium ion batteries and solar cells due to its high electric conductivity (1×10^4 S m^{-1})[28–34]. However, compared with graphene, to the best of our knowledge no detailed study has been conducted. Hence, we have conducted a systematic computational study on the 2D TiS_2–MoS_2 (ML) contacts by using first-principles simulation. We found that the intrinsic structure of ML MoS_2 is well preserved after forming a contact with TiS_2. As shown in Fig. 1b, c, the TiS_2 contact induces ML MoS_2 to demonstrate *p*-type behavior, while graphene contact induces it to become *n*-doped[35]. Another interesting finding from our study is that the Schottky barrier height for the TiS_2 contact and ML MoS_2 changes by varying the doping type and concentration of MoS_2. By using the projected local device density of states (PLDOS) analysis, we have extracted the barrier heights of TiS_2–MoS_2 (ML) contacts at different doping type and concentrations along with different TiS_2 thickness. We found that, for intrinsic and *n*-type-doped ML MoS_2, TiS_2 forms a Schottky contact

[1]Department of Electrical and Computer Engineering, University of Alberta, Edmonton, AB, Canada. ✉email: mgupta1@ualberta.ca

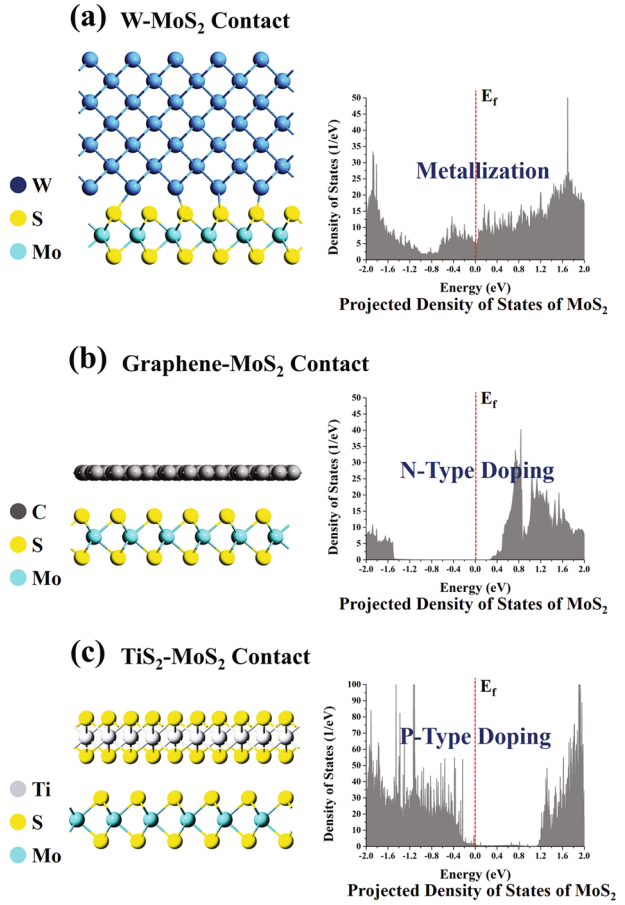

Fig. 1 ML MoS_2 contact formation with tungsten (W), graphene, and TiS_2. Contact geometry is shown in **a**–**c** along with respective PDOS for W–ML MoS_2 contact, Graphene–ML MoS_2 contact, and TiS_2–ML MoS_2 contact. The results for metal[14,15] and graphene contact are obtained from our simulations and agree with the reported experimental data[14,18,35]. It indicates that metal contact adds metallization to ML MoS_2 and bandgap of MoS_2 vanishes. Graphene and TiS_2 contacts preserve the bandgap, due to the van der Waal forces, ML MoS_2 but add *n*-type and *p*-type dopings, respectively.

whereas for *p*-type ML MoS_2, TiS_2 forms an ohmic contact. Thus, we can use TiS_2 to obtain high-quality ohmic and Schottky contacts for ML MoS_2 for fabrication of high-quality devices.

RESULTS

TiS_2 contact formation with ML MoS_2

The "Methods" section describes the density functional theory (DFT) techniques used for this research. The contact formation between TiS_2–MoS_2 leads to two interfaces as seen in Fig. 2d. To confirm this, two geometries are adopted to investigate the contact, which are shown in Fig. 2a, b. A group of TiS_2–MoS_2 junctions are used to test the electron transport from TiS_2 contact to the ML MoS_2 sheet at the lateral interface (interface A in Fig. 2d). Another group of FET-like TiS_2–MoS_2 heterostructures (TiS_2–MoS_2 FET-like junctions) are used to simulate the electron transportation from the contact region to semiconducting channel region at the vertical interface (interface B in Fig. 2d).

For TiS_2–MoS_2 FET-like junction, the PLDOS is calculated for revealing the band structure after the contacting of 1–4 layers of TiS_2 and ML MoS_2 sheet. The configuration after geometrical optimization (GO) is shown by Fig. 2d. The overlap of 1–4 layers of TiS_2 and ML MoS_2 is 2.5 nm. Due to the limitation of computational capability, the ML-MoS_2 channel is set as 8 nm. To increase the accuracy in the transportation direction, the *k*-point sampling is changed to $10 \times 1 \times 40$. For each of 1–4 layers of TiS_2 simulations, The MoS_2 channel doping is varied to understand the type of electrode formation as 5×10^{18} cm^{-3} (3.25×10^{11} cm^{-2} for ML MoS_2) *n*-type doping, 1×10^{19} cm^{-3} (6.5×10^{11} cm^{-2} for ML MoS_2) *n*-type doping, 5×10^{19} cm^{-3} (3.25×10^{12} cm^{-2} for ML MoS_2) *n*-type doping, and 5×10^{18} cm^{-3} (3.25×10^{11} cm^{-2} for ML MoS_2) *p*-type doping. Thus, we obtain a n_i value of 1.4×10^4 cm^{-3} for ML MoS_2. We chose the doping concentration carefully to meet the calculated upper and lower limits: a large doping concentration will lead to degenerate behavior of the channel and a small doping concentration will cause the depletion length to exceed the length of channel creating artificial results. The overlap region between the TiS_2 and MoS_2 is undoped. Only the uncovered ML-MoS_2 channel is doped with the chosen doping concentrations.

To investigate the charge transport and its mechanism through the interface A in Fig. 2d, the calculation of DOS, ED, average binding energy (EBE), and EDP are conducted after the GO.

After simulating the DOS of the optimized TiS_2–MoS_2 structure, the projected partial DOS (PDOS) is shown in Fig. 3. The PDOS of TiS_2 after making contact with ML MoS_2 is shown in Fig. 3a–d for one–four layers of TiS_2. It shows that, after making a contact with ML MoS_2, the TiS_2 DOS remains the same as the free-standing TiS_2. The only difference is that some trap states are added which shown as spikes in Fig. 3a–d. These added states are created by the tiny displacement of the atoms in TiS_2 layer, which is of the order of 0.01 Å. This indicates that the presence of ML MoS_2 has a negligible effect on the TiS_2 band structure. The situation of MoS_2 is different, as shown in Fig. 3e–i which show the PDOS of ML MoS_2 after making contact with one–four layers of TiS_2. The plot clearly demonstrates that the TiS_2 contact modifies the MoS_2 band structure significantly and adds a large amount of *p*-type doping to the ML MoS_2. In Fig. 3e–i, compared with the band structure and DOS of intrinsic ML MoS_2 on the left side, for all the cases of ML to four-layer TiS_2 contacts, the PDOS of ML MoS_2 exhibits Fermi level pinning towards valence band. This shift of Fermi level ranges from 0.40 to 0.45 eV. Even though the three-layer and four-layer TiS_2 forming a contact with ML MoS_2 show a larger Fermi level shift, the difference in Fermi level shift with change in number of TiS_2 layers is very small. The energy difference between the valence band and Fermi level is 0.05–0.1 eV. The energy difference between the Fermi level and valence band is defined by

$$\Phi = E_f - E_V, \tag{1}$$

where E_f and E_V are the Fermi level and the valence band top, respectively. Knowing the Fermi level shift and Φ, the *p*-type doping concentration can be determined by calculating the effective DOS in the conduction band (N_c) and the valence band (N_v). As there are not too many reported values of N_c and N_v reported, we have calculated these to estimate what doping concentration we should use for our electrode simulations for ML MoS_2. Hence, the effective density of state values is required only for estimating the doping concentrations of MoS_2. After simulating the DOS, the energy difference between the quasi-Fermi level and the valence band can be calculated. These two well-defined equations can be applied to determine N_c and N_v:

$$N_c = n \exp\left(\frac{E_c - E_F}{kT}\right), \tag{2}$$

$$N_v = p \exp\left(\frac{E_F - E_v}{kT}\right), \tag{3}$$

where *n* and *p* are the electron and hole concentrations, respectively. *k* is Boltzmann constant and *T* is temperature in *K*. From the simulation, N_c and N_v for ML MoS_2 are calculated to be 2×10^{19} cm^{-3} (1.38×10^{12} cm^{-2}) and 1×10^{19} cm^{-3} (6.5×10^{12} cm^{-2}), respectively,

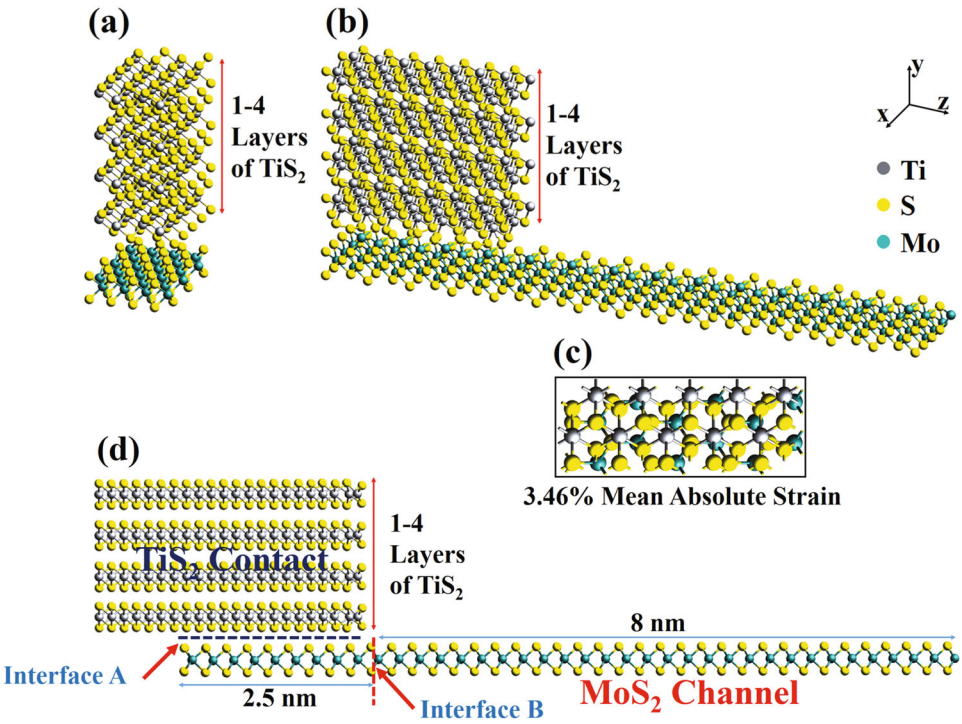

Fig. 2 Geometry set-up for TiS_2–MoS_2 contacts. a TiS_2–MoS_2 junction, where the gray, blue. and yellow balls represent Ti, Mo, and S atoms, respectively. **b** TiS_2–MoS_2 FET-like structure. **c** Top view of (001) TiS_2 surface on monolayer (001) MoS_2 surface. **d** Parameter set-up for (1–4 layers of) TiS_2–MoS_2 FET-like junctions. Here, the interface A shows the lateral interface, which lies between the TiS_2 contact and ML MoS_2. The interface B shows the vertical interface, which lies between the contact region and the MoS_2 channel.

which are similar to the reported ML and bulk MoS_2 values[36–39]. Using these values, the calculated doping concentration added to the ML MoS_2 by TiS_2 contacts with different number of layers ranges from 3.85×10^{17} to 2.63×10^{18} cm^{-3} (2.50×10^{10} to 1.71×10^{11} cm^{-2} for ML MoS_2). Compared with metal–MoS_2 contacts[14–18], although the ML MoS_2 is *p*-type doped after forming a contact with TiS_2, its bandgap is preserved as shown in Fig. 3e–i; in contrast, the metal contact will metalize the ML MoS_2 and fill its bandgap with states as shown in Fig. 1a. The TiS_2–MoS_2(ML) contact makes ML MoS_2 *p*-type as compared to the *n*-type in graphene–MoS_2 contact (Fig. 1b).

Thus, the DOS simulation indicates that TiS_2–MoS_2 (ML) contact is a unique contact with less metallization and *p*-type behavior. It is necessary to conduct a comprehensive analysis on its interfacial bonding condition. ED and EBE are two important criteria to evaluate the bonding between TiS_2 and ML MoS_2. The average binding energy (EBE), E_B, can be defined as

$$E_B = (E_T + E_M - E_{T-M})/N, \quad (4)$$

where E_T is the total energy of the free-standing TiS_2, E_M is the total energy of the intrinsic ML MoS_2, E_{T-M} is the total energy of the TiS_2–MoS_2 (ML) contact after GO, and N can be considered as the number of interfacial sulfur atoms on the MoS_2 side.

The ED of the TiS_2–MoS_2 junctions are shown by Fig. 4a–d for one–four layers of TiS_2. As seen in the plot, there is a clear gap between the TiS_2 layer and MoS_2 with no charge distribution in it. The overlap of the electron gas between TiS_2 and MoS_2 is very limited, as can be observed from the contour plot. The plot of the projected electron density (ED) in the *y* direction also clearly shows that the ED overlap at the contact interface is very similar to those between TiS_2 layers, indicating that the bonding between TiS_2 and MoS_2 is not much stronger than interfacial bonding within TiS_2 layers. The buckling distance can also be extracted from both the ED plot and GO. For TiS_2–MoS_2(ML) junctions, the optimized buckling distance for TiS_2–MoS_2 contacts are: 3.2282 Å for TiS_2(ML)–MoS_2(ML), 2.8112 Å for TiS_2(2L)–MoS_2(ML), 2.8069 Å for TiS_2(3L)–MoS_2 (ML), and 2.7381 Å for TiS_2(4L)–MoS_2(ML). For comparison, the inter-layer distance for TiS_2 and MoS_2 is 2.8678 and 2.9754 Å, respectively. It is clear that thicker TiS_2 has larger attractive force to ML MoS_2 and leads to smaller inter-layer distance. These ED results reveal that the bonding between the TiS_2 contact and ML MoS_2 in TiS_2–MoS_2 (ML) junctions is Van der Waals bonding. Unlike the covalent bond, the delocalization of interfacial electron gas would not exist in these cases.

By using this definition, the EBE for TiS_2–MoS_2(ML) interface is 0.7426 eV, while this value is 0.7157 eV for the Van der Waals bonds of bilayer MoS_2. This result further confirms the previous results and demonstrates that TiS_2–MoS_2 (ML) contact is a Van der Waals contact.

The tunneling barrier at the TiS_2–MoS_2 (ML) interface will determine the charge transport through the interface A. To evaluate the impedance to the current transportation added by the tunneling barrier, the electrostatic difference potential (EDP) of the TiS_2–MoS_2 contact is simulated. As shown in Fig. 4e, the potential between the TiS_2 and MoS_2 is considered as the tunneling barrier. The shape of the potential barrier can be estimated as a rectangle. The tunneling probability, from the TiS_2 to the ML MoS_2 can be defined as, of carriers tunneling through the barrier, T_B

$$T_B = \exp\left(-4\pi \frac{\sqrt{2m\Delta V}}{h} W_B\right), \quad (5)$$

where ΔV is the barrier height, which is defined by the length of the rectangle, h is the Planck constant, and W_B is the barrier width, which is defined as the half width of the rectangle. ΔV and W_B can be directly extracted from Fig. 4e: ΔV is 0.404620 eV and W_B is 0.35412 Å. By using these parameters and Eq. (4), we calculate T_B as 79.4%. A large T_B indicate small impedance and a higher charge injection. It is very clear that even though the tunneling barrier at the interface A resists the charge transport vertically through the interface, the possibility of tunneling is high for carriers because of a

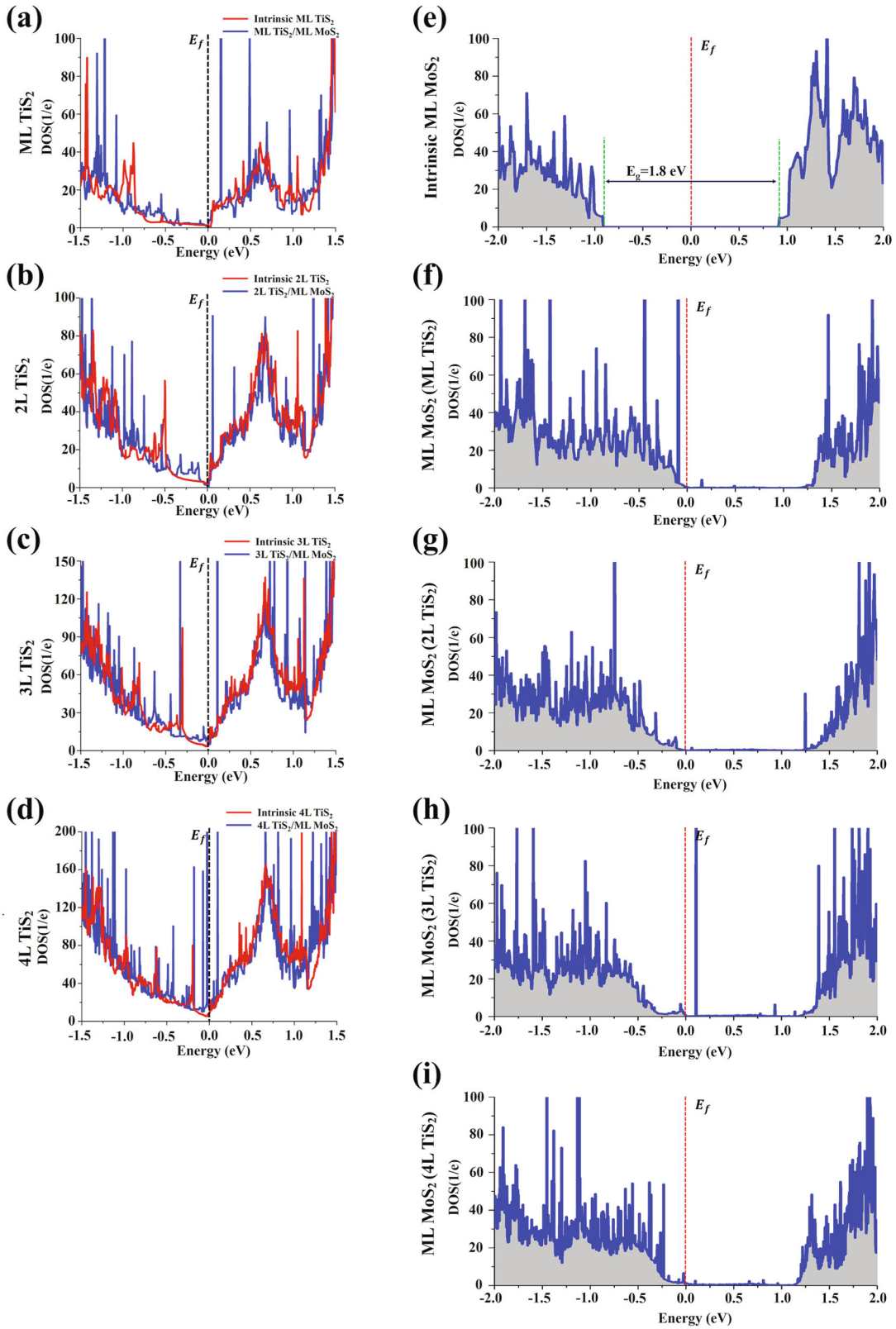

Fig. 3 The partial density of states (PDOS) of TiS_2 and MoS_2 within TiS_2(ML to 4L)–MoS_2(ML) contacts. a–d PDOS of TiS_2 (from ML to 4L). In the plot, the dashed line indicates the position of Fermi level, which is set as zero point. The red line represents the DOS of free-standing TiS_2, as a comparison. **e–i** PDOS of ML MoS_2. On the top is the DOS of free-standing ML MoS_2, as a comparison. The Fermi level of each plot has been aligned to the same energy value. The label ML-TiS_2 to 4L-TiS_2 indicate the TiS_2 contact thickness.

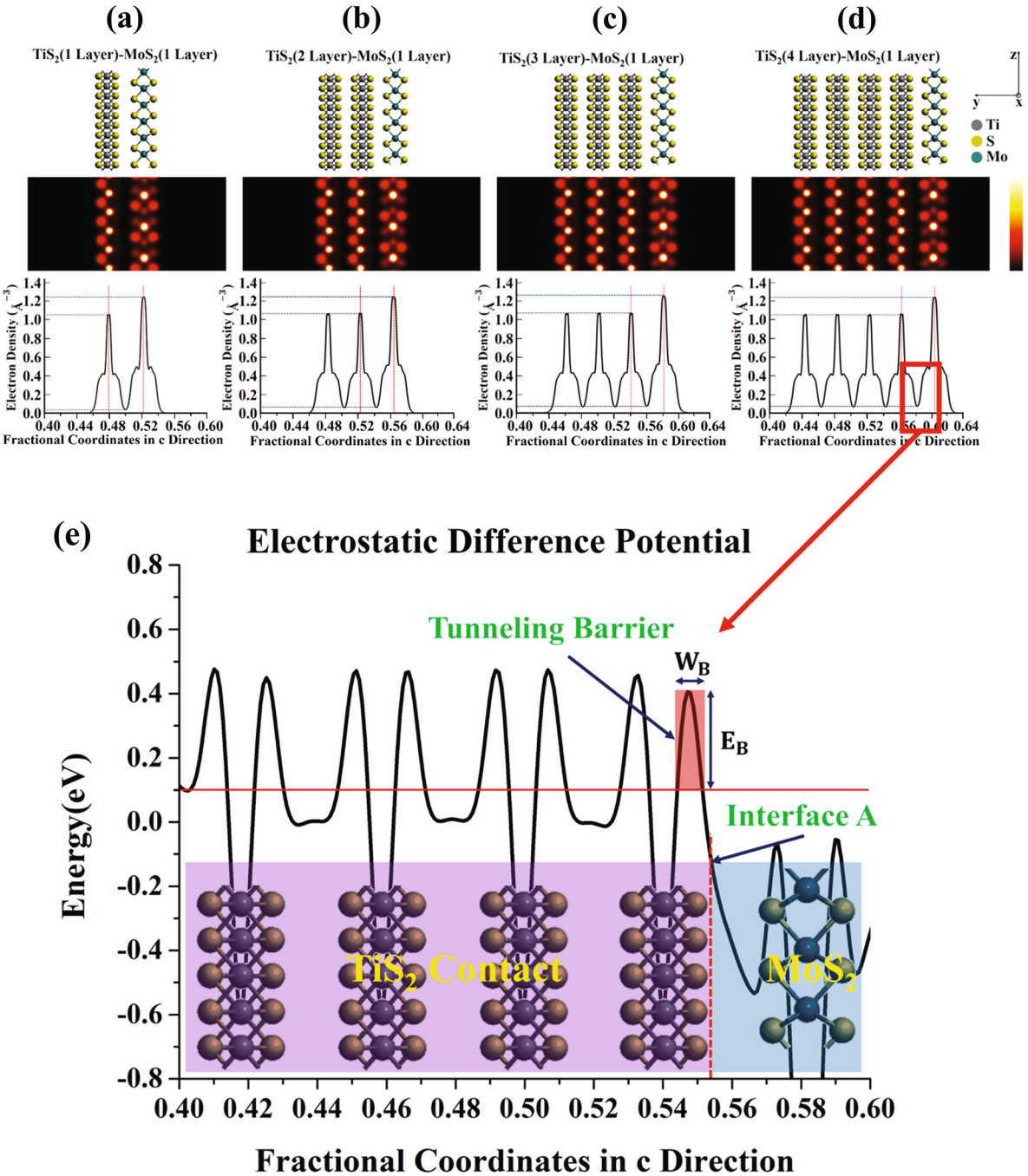

Fig. 4 Electron density (ED) and electrostatic difference potential (EDP) of TiS_2–ML MoS_2 junctions. a–d ED on the top is the configuration after GO. The middle one is the contour plot of the ED with brighter color indicating higher ED. The bottom plot is for the normalized ED projected on the *y* direction (vertical to the contact plane). **e** EDP, *x*-axis is the fractional coordinates of 8 nm long superlattice along the *c* direction. The geometry configuration is integrated in the plot, which is shown on the bottom. It shows that at the interface A, there is a small tunneling barrier. The scale bar is from 0.0 to 3.0 ($Å^{-3}$).

very tiny barrier width (0.35412 Å). For this reason, the charge injection at the lateral interface can be ignored. However, the interfacial tunneling barrier within the TiS_2 contact may scatter the electrons and holes. This scattering effect can be reduced by using a thinner TiS_2 film. Thus, we also address scaling down the thickness of TiS_2 contacts after meeting the stability requirement.

By analyzing the ED, EBE, and GO for configuration for interface A, it can be concluded that TiS_2 tends to form Van der Waals bond with ML MoS_2, with thicker TiS_2 creating stronger bonding. The DOS in Fig. 3 shows that less metallization is created due to the weak Van der Waals bonding and the bandgap of ML MoS_2 is preserved. DOS results also show that TiS_2 will add *p*-type doping to the ML MoS_2. The EDP results in Fig. 4 show that the tunneling barrier is small at interface A, which means that the current injection would not be seriously impeded.

To understand the source-to-channel/channel-to-drain working mechanism for the TiS_2–MoS_2 (ML) contacts applied in 2D FET, the PLDOS is adopted to sketch out the framework of the band structure at the interface B of the TiS_2–MoS_2 FET-like junctions. The PLDOS uses a contour plot to map the DOS projected onto

Table 1. Calculated depletion wdth W_D, vertical barrier height for electrons Φ_n, and vertical barrier height for holes Φ_p for the TiS_2 with different number of layers and ML MoS_2 junction.

Number of TiS_2 layers/ML MoS_2 doping conc. and type	Depletion width W_D (nm)	Vertical barrier height for electrons Φ_n (eV)	Vertical barrier height for holes Φ_p (eV)	Effective band gap after formation of junction E_g (eV)
1L, 5×10^{18} (*p*-type)	–	1.35	0.13	1.48
2L, 5×10^{18} (*p*-type)	–	1.18	0.05	1.23
3L, 5×10^{18} (*p*-type)	–	1.18	0	1.18
4L, 5×10^{18} (*p*-type)	–	1.18	0	1.18
1L, 5×10^{18} (*n*-type)	6.4	1.03	0.67	1.70
2L, 5×10^{18} (*n*-type)	6.3	1.05	0.21	1.26
3L, 5×10^{18} (*n*-type)	5.8	1.07	0.25	1.32
4L, 5×10^{18} (*n*-type)	5.8	1.03	0.23	1.26
1L, 1×10^{19} (*n*-type)	3.6	0.95	0.70	1.65
2L, 1×10^{19} (*n*-type)	4.9	0.92	0.40	1.32
3L, 1×10^{19} (*n*-type)	4.6	0.90	0.42	1.32
4L, 1×10^{19} (*n*-type)	4.8	0.88	0.44	1.32
1L, 5×10^{19} (*n*-type)	1.6	0.35	0.95	1.30
2L, 5×10^{19} (*n*-type)	1.5	0.45	0.92	1.37
3L, 5×10^{19} (*n*-type)	1.2	0.30	0.97	1.27
4L, 5×10^{19} (*n*-type)	1.2	0.30	0.97	1.27

the *c*-axis, which is the transportation direction. The band structure can be determined by plotting the boundary between the states-filled region (bright region) and the no-states region (dark region). The extraction of the barrier height and contact type of TiS_2–MoS_2 contact can be achieved by evaluating the PLDOS. Two reasons let us dope the ML MoS_2. First, the intrinsic carrier concentration of ML MoS_2 is small; therefore, it is a good choice to dope the MoS_2 channel to improve the conductivity. For this reason, it is of great interest to investigate the contact consisting of doped ML MoS_2. Also, the channel length is set to 8 nm based on computational considerations, as mentioned earlier. An adequate amount of doping concentration is required to make sure that the depletion length is smaller than the channel length of the simulated configuration. Although the barrier height and contact type for the contact of intrinsic ML MoS_2 and TiS_2 cannot be extracted directly from the PLDOS, but the barrier height and contact type of doped cases can still be extracted accurately.

MoS_2 doping-dependent contact formation with TiS_2

Four different doping concentrations: 5×10^{18}, 1×10^{19}, and $5\times10^{19}\,cm^{-3}$ *n*-type doping and $5\times10^{18}\,cm^{-3}$ *p*-type doping is tested. The simulation results are shown in Table 1. Figure 5 shows only the results of the TiS_2(4L)–MoS_2(ML) cases and the variation of the band structures with different doping concentrations.

For *n*-type doping concentrations smaller than N_c, the Schottky barrier height of the contacts are large: 1.03–1.07 eV for $5\times10^{18}\,cm^{-3}$, and 0.88–0.95 eV for $1\times10^{19}\,cm^{-3}$, as shown in Table 1 and Fig. 5b, c. Table 1 also clearly shows that for the cases with ML TiS_2, Φ_p of the contact is larger than Φ_p of 2L–4L cases with the same doping concentration. For the *n*-type doping concentration of $5\times10^{18}\,cm^{-3}$, Φ_p is 0.67 eV for ML but 0.21–0.25 eV for 2–4L. For *n*-type doping concentration of $1\times10^{19}\,cm^{-3}$, Φ_p is 0.7 eV for ML but 0.40–0.44 eV for 2–4L. By summing Φ_n and Φ_p, the modified E_g is 1.70 eV for the ML case doped *n*-type with concentration $5\times10^{18}\,cm^{-3}$, and for 2–4L cases doped with this concentration, E_g ranges from 1.26 to 1.32 eV. For *n*-type doping of concentration $1\times10^{19}\,cm^{-3}$, E_g is 1.65 eV for ML and 1.32 eV for 2–4L.

For a larger *n*-type doping concentration ($5\times10^{19}\,cm^{-3}$), as shown in both Table 1 and Fig. 5a, the Schottky barrier height is 0.30–0.45 eV, which is much smaller than the cases with *n*-type doping concentrations of 5×10^{18} and $1\times10^{19}\,cm^{-3}$. This reduction in barrier height may be brought about by multiple causes. One possible reason is the imaging force created by the larger amount of excess charge, as a result of the larger doping concentration. It is observed that Φ_p increases compared with lower doping concentrations. Φ_p is 0.92–0.97 eV for the 1–4L cases. E_g for this concentration is 1.27–1.37 eV.

The simulation results and mapped band structures in Fig. 5a–c for *n*-type-doped TiS_2–MoS_2(ML) contacts show that, normally, *n*-type-doped TiS_2–MoS_2(ML) contacts show a large barrier height, which is around 1.0 eV below a degenerate doping. Even though Fig. 5 shows that a larger doping concentration will reduce the barrier height for *n*-type carriers, it is obvious that, even for a doping concentration very close to degeneration, the Schottky barrier height is still larger for TiS_2–MoS_2(ML) contacts. The inference from Fig. 5 is that since the majority carriers in these *n*-type-doped contacts are always faced with a large Schottky barrier height, the *n*-type-doped TiS_2–ML MoS_2 Schottky diodes can probably act as high-power switches or Schottky barrier MOSFETs based on tunneling.

Unlike the *n*-type contacts, the *p*-type-doped TiS_2–MoS_2(ML) contacts shows zero barrier height when the *p*-type doping concentration reaches $5\times10^{18}\,cm^{-3}$. In Fig. 5d, it is observed that, at this doping concentration, the depletion width vanishes and the band is flat. The Schottky barrier at the interface shows both a small barrier height and a small built-in potential, which indicates the contact is an ohmic contact for ML MoS_2-doped *p*-type at a concentration of $5\times10^{18}\,cm^{-3}$.

For the cases with *p*-type doping concentration of $5\times10^{18}\,cm^{-3}$, only the ML and 2L cases show a very small barrier height Φ_p (0.13 eV for ML and 0.05 eV for 2L). For the 3L and 4L cases, there is zero barrier height. Φ_n is 1.35 eV for ML and 1.18 eV for 2–4L, as shown in Table 1. For the cases with *p*-type doping concentration of $5\times10^{18}\,cm^{-3}$, the bandgap shrinks to 1.48 eV for ML TiS_2 and 1.18 eV for 2–4L.

As inferred from Fig. 5d, when the doping is *p*-type with a concentration of $5\times10^{18}\,cm^{-3}$, the contact is ohmic for *p*-type carriers while the barrier for *n*-type carriers is still large. As mentioned earlier, the doping concentration P_c was added to the ML MoS_2 within the contact region ranges from 3.85×10^{17} to $2.63\times10^{18}\,cm^{-3}$. When the *p*-type doping of channel MoS_2 reaches the value of P_c, the band will become flat, and the contact

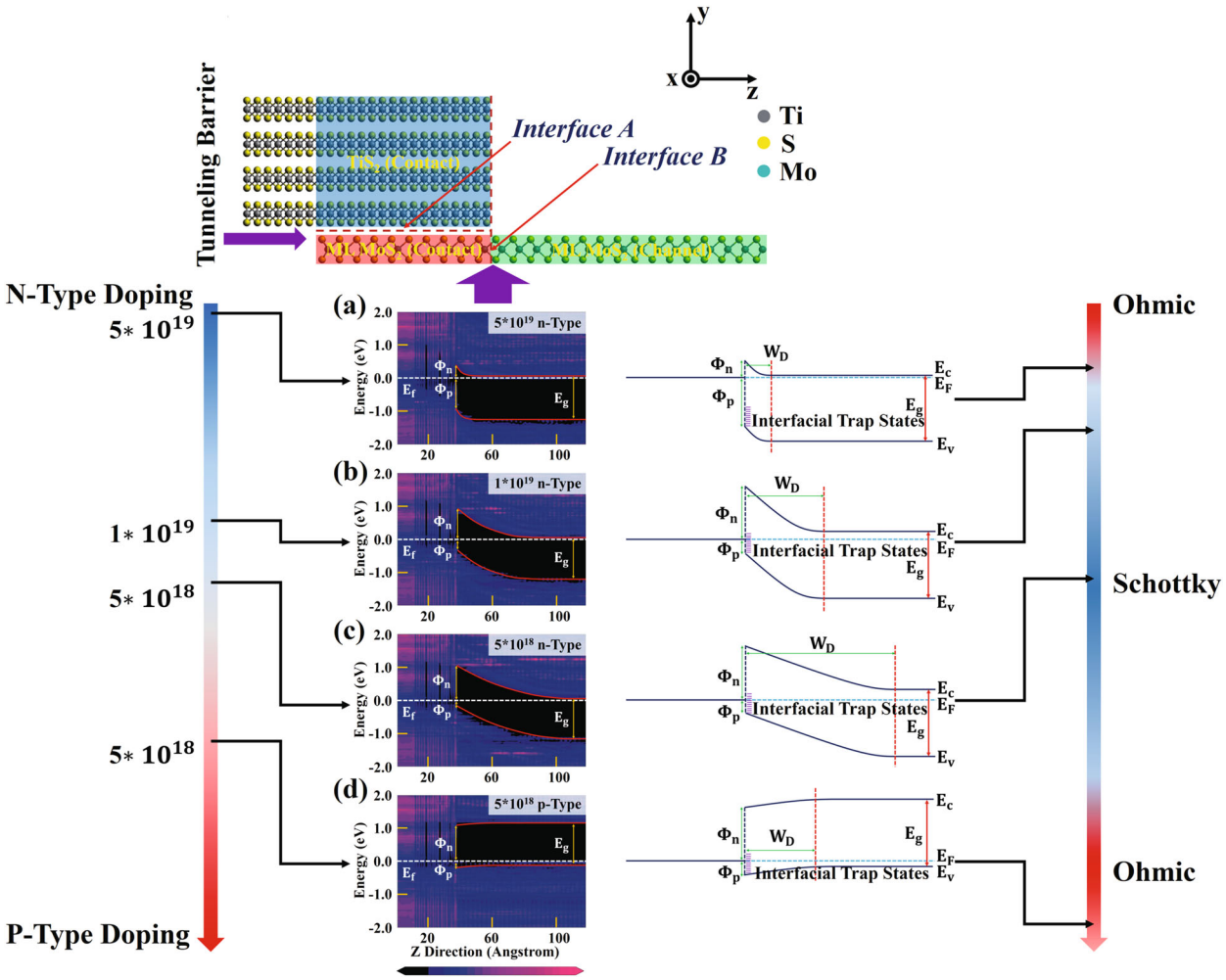

Fig. 5 PLDOS of TiS_2–MoS_2(ML) FET-like junctions doped with different doping concentrations and the variation of band structure at interface B. a–d The doping concentrations are: $N = 5 \times 10^{19}$ cm^{-3}, $N = 1 \times 10^{19}$ cm^{-3}, $N = 5 \times 10^{18}$ cm^{-3}, and $P = 5 \times 10^{18}$ cm^{-3}. The thickness of TiS_2 is four layers. On the right-side, the plot shows the variation of band structure under different doping concentrations. The scale bar is from 0.0 to 90.0 (1/eV).

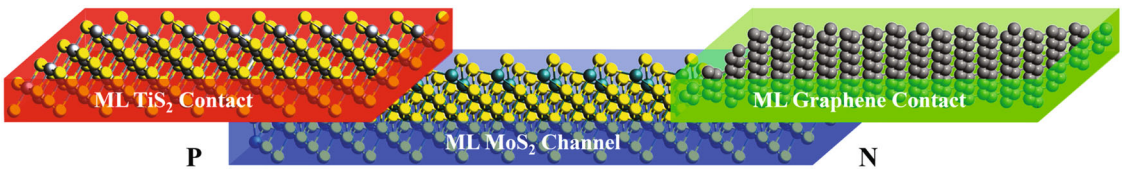

Fig. 6 Schematic of TiS_2–MoS_2–graphene heterostructure device. TiS_2 and graphene act as 2D contacts as the contact formation will induce *p*-type and *n*-type doping on the two sides of ML MoS_2 channel, respectively.

becomes an ohmic contact. Thus, TiS_2 can be used as an either an ohmic or Schottky contact depending on the doping of the ML MoS_2.

DISCUSSIONS

We propose a design for a ML MoS_2 with two different contacts namely TiS_2 on one side and graphene on the other to achieve tunable functionalities as shown in the schematic in Fig. 6. Since TiS_2 junction with ML MoS_2 induces *p*-type doping, while graphene contact induces *n*-type doping as reported[35]. The heterostructure shown in Fig. 6 consists of TiS_2 contact on the left side and graphene contact on the right with ML MoS_2 channel. The working principle of the device depends on the doping condition of the channel. If the channel is *p*-type doped, it tends to form Ohmic contact with graphene while forming a Schottky contact on the right side. This would flip if the channel is *n*-type. This device would turn on only if the Schottky barrier is overcome. In addition, if an oxide and gate are added to the MoS_2 to obtain better control over the channel. This device can be made using *p* and *n*-type ML MoS_2 doping using the same materials for electrode and obtain complementary devices. In addition, from our simulation studies, we observe that the covalent-bonding contacts add metallization to the MoS_2. Thus, for a good contact that preserves the doping concentration of the MoS_2 one would prefer a material which forms van der Waal bond with it although

it will introduce some loss due to the inter-layer impedance. Hence, one can utilize 2D materials to obtain high performance devices.

Using the first-principle DFT simulation, a comprehensive and detailed study on TiS_2–(ML) MoS_2 contact has been conducted. The simulation shows that, unlike most other contact materials, it is unique that the presence of a TiS_2 contact adds *p*-type doping to the ML MoS_2 sheet. The Fermi level shift and smaller metallization effect in the contact region preserves the intrinsic nature of ML MoS_2. A tunneling barrier model is employed and we have extracted the transmission rate by using quantum mechanical calculations. The transmission rate T_B (79.4%) is very high at the interface. However, thinner contacts are necessary to reduce carrier scattering. We thus observe that TiS_2 forms a *n*-type Schottky contact with intrinsic ML MoS_2 at the vertical interface, but the barrier heights for both electrons and holes are large. The barrier height for electrons (Φ_n) and the holes (Φ_p) at vertical interface can be reduced having either *n*-type or *p*-type doping in the channel region. The barrier height is small for *p*-type-doped channels and TiS_2 can form either an ohmic contact or a Schottky contact with low barrier height, which depends on the *p*-type doping concentration of MoS_2. Thus, our simulation results demonstrate that TiS_2 is a promising 2D electrode material for ML MoS_2, because it does not distort the structure of the ML MoS_2 much as compared to the metals which metallize the MoS_2 strongly. This merit makes TiS_2 contact viable for a variety of applications for ML MoS_2 heterostructure devices like *p*–*n* hetero device. Also, in addition to its utility as a good electrode material TiS_2 also can be used as a *p*-type dopant for MoS_2.

METHODS

Density functional theory

The computational study based on DFT[40] has been conducted for this research using Atomistix ToolKit (ATK)[41]. For all the simulations, TiS_2–MoS_2 junctions and TiS_2–MoS_2 FET-like junctions, the thickness of the TiS_2 was chosen to range from ML to 4L (four layers) to explore the impact created by the variation of the TiS_2 thickness, while the MoS_2 channel is set as ML. The mean absolute strain is set as 3.46% for the lattice mismatch between the TiS_2 layer and ML MoS_2 for the simulations. It means the $5\times\sqrt{3}$ unit cell of the Ti matches the $3\sqrt{3}\times 2$ unit cell of ML MoS_2. The Ti atoms in the TiS_2 layer occupy both on-top sites and hollow sites of the MoS_2 layer. This combination gives a much smaller total energy compared with the pure on-top configuration (which is possible for TiS_2 and MoS_2 because both of them are TMDCs). Since the periodic boundary condition (PBC) is applied in the simulation, a vacuum buffer of 30 Å is added in vertical direction to both groups of configurations to let the electrostatic potential decay softly at the boundary.

Perdew–Burke–Ernzerhof variant of generalized gradient approximation (GGA)[42] is applied for the DFT calculation. For simulation, the Hartwigsen–Goedecker–Hutter (HGH)[43] basis set is adopted to expand the ED. A DFT-D2[44] correction is applied to make a correction to the interfacial Van der Waals bonding. Since the spin–orbital interaction is not taken into consideration in our simulation no correction was applied for it. The *k*-point sampling for TiS_2–MoS_2 junction is $12\times4\times1$ while it is $10\times1\times1$ for TiS_2–MoS_2 FET-like junction. All the *k*-point samplings are defined after a convergence test, which ensures that the total energy is converged to $<1.0\times10^{-5}$ eV. By conducting the convergence test, the energy cut-off for the simulation is set as 200 Ry. The maximum force, which determines the convergence of the geometry optimization (GO), is set as 0.05 eV $Å^{-1}$. The DOS, ED, and EDP also have been conducted utilizing this set-up.

DATA AVAILABILITY

The data that support the findings of this study are available from the corresponding author upon request.

Received: 30 March 2020; Accepted: 8 July 2020;
Published online: 31 July 2020

REFERENCES

1. Radisavljevic, B., Radenovic, A., Brivio, J., Giacometti, V. & Kis, A. Single-layer MoS2 transistors. *Nat. Nanotechnol.* **6**, 147–150 (2011).
2. Pradhan, S. K., Xiao, B. & Pradhan, A. K. Enhanced photo-response in p-Si/MoS2 heterojunction-based solar cells. *Sol. Energy Mater. Sol. Cells* **144**, 117–127 (2016).
3. Cho, B. et al. Chemical sensing of 2D graphene/MoS2 heterostructure device. *ACS Appl. Mater. Interfaces* **7**, 16775–16780 (2015).
4. Nan, H. et al. Improving the electrical performance of MoS2 by mild oxygen plasma treatment. *J. Phys. D* **50**, 154001 (2017).
5. Sung, H. J., Sung, H.-J., Choe, D.-H. & Chang, K. J. The effects of surface polarity and dangling bonds on the electronic properties of monolayer and bilayer MoS2 on α-quartz. *New J. Phys.* **16**, 113055 (2014).
6. Kam, K. K. & Parkinson, B. A. Detailed photocurrent spectroscopy of the semiconducting group VI transition metal dichalcogenides. *J. Phys. Chem.* **86**, 463–467 (1982).
7. Cui, X. et al. Multi-terminal transport measurements of MoS2 using a van der Waals heterostructure device platform. *Nat. Nanotechnol.* **10**, 534–540 (2015).
8. Pu, J. et al. Highly flexible MoS2 thin-film transistors with ion gel dielectrics. *Nano Lett.* **12**, 4013–4017 (2012).
9. Liu, H. & Ye, P. D. MoS2 dual-gate MOSFET with atomic-layer-deposited Al2O3 as top-gate dielectric. *IEEE Electron Device Lett.* **33**, 546–548 (2012).
10. Zhan, Y., Liu, Z., Najmaei, S., Ajayan, P. M. & Lou, J. Large-area vapor-phase growth and characterization of MoS2 atomic layers on a SiO2 substrate. *Small* **8**, 966–971 (2012).
11. Wang, H. et al. Integrated circuits based on bilayer MoS2 transistors. *Nano Lett.* **12**, 4674–4680 (2012).
12. Cho, A. J. et al. Multi-layer MoS2 FET with small hysteresis by using atomic layer deposition Al2O3 as gate insulator. *ECS Solid State Lett.* **3**, 67–69 (2014).
13. Yu, L. et al. Enhancement-mode single-layer CVD MoS2 FET technology for digital electronics. *2015 IEEE International Electron Devices Meeting (IEDM)*, 32.3.1–32.3.4 (Washington, DC, 2015). https://doi.org/10.1109/IEDM.2015.7409814.
14. Gao, J., Nandi, D. & Gupta, M. Density functional theory-projected local density of states-based estimation of Schottky barrier for monolayer MoS2. *J. Appl. Phys.* **124**, 014502 (2018).
15. Zhong, H. et al. Interfacial properties of monolayer and bilayer MoS2 contacts with metals: beyond the energy band calculations. *Sci. Rep.* **6**, 21786 (2016).
16. Kang, J., Liu, W., Sarkar, W., Jena, D. & Banerjee, K. Computational study of metal contacts to monolayer transition-metal dichalcogenide semiconductors. *Phys. Rev. X* **4**, 1–14 (2014).
17. Kang, J., Liu, W. & Banerjee, K. High-performance MoS2 transistors with low-resistance molybdenum contacts. *Appl. Phys. Lett.* **104**, 093106 (2014).
18. Kaushik, N. et al. Schottky barrier heights for Au and Pd contacts to MoS2. *Appl. Phys. Lett.* **105**, 1–5 (2014).
19. Han, X., Lin, J., Liu, J., Wang, N. & Pan, D. Effects of hexagonal boron nitride encapsulation on the electronic structure of few-layer MoS2. *J. Phys. Chem. C* **123**, 14797–14802 (2019).
20. Vu, Q. A. et al. Near-zero hysteresis and near-ideal subthreshold swing in h-BN encapsulated single-layer MoS2 field-effect transistors. *2D Mater.* **5**, 031001 (2018).
21. Yoon, J. et al. Highly flexible and transparent multilayer MoS2 transistors with graphene electrodes. *Small* **9**, 3295–3300 (2013).
22. Liu, Y. et al. Toward barrier free contact to molybdenum disulfide using graphene electrodes. *Nano Lett.* **15**, 3030–3034 (2015).
23. Shin, H. G. et al. Vertical and in-plane current devices using NbS2/n-MoS2 van der Waals Schottky junction and graphene contact. *Nano Lett.* **18**, 1937–1945 (2018).
24. Chuang, H. J. et al. Low-resistance 2D/2D ohmic contacts: a universal approach to high-performance WSe2, MoS2, and MoSe2 transistors. *Nano Lett.* **16**, 1896–1902 (2016).
25. Xie, L. et al. Graphene-contacted ultrashort channel monolayer MoS2 transistors. *Adv. Mater.* **29**, 1–7 (2017).
26. Drube, W., Schafer, I. & Skibowski, M. The experimental band structure of occupied and unoccupied states of titanium dichalcogenides. *J. Phys. C* **20**, 4201 (1987).
27. Yukimasa, Y. & Motizuki, K. Electron-lattice interactions and lattice instabilities of 1T-VSe2, 1T-CrSe2 and 1T-TiS2. *J. Phys. Soc. Jpn.* **51**, 2107–2115 (1982).
28. Chen, J., Tao, Z.-L. & Li, S.-L. Lithium intercalation in open-ended TiS2 nanotubes. *Angew. Chem.-Int. Ed.* **42**, 2147–2151 (2003).
29. Fujii, Y. et al. Reaction mechanism of FePS3 electrodes in all-solid-state lithium secondary batteries using sulfide-based solid electrolytes. *J. Electrochem. Soc.* **165**, A2948–A2954 (2018).
30. Huckaba, A. J. et al. Low-cost TiS2 as hole-transport material for perovskite solar cells. *Small Methods* **1**, 1700250 (2017).
31. Verrelli, R. et al. Steps towards the use of TiS2 electrodes in Ca batteries. *J. Electrochem. Soc.* **167**, 070532 (2020).
32. Lickleder, M., Cha, G., Hahn, R. & Schmuki, P. Ordered nanotubular titanium disulfide (TiS2) structures: synthesis and use as counter electrodes in dye sensitized solar cells (DSSCs). *J. Electrochem. Soc.* **166**, H3009–H3013 (2019).

33. Wang, L. et al. TiS2 as a high-performance potassium ion battery cathode in ether-based electrolyte. *Energy Storage Mater.* **12**, 216–222 (2018).
34. Ferhat, S. et al. Flexible thermoelectric device based on TiS2(HA)x n-type nanocomposite printed on paper. *Org. Electron.* **68**, 256–263 (2019).
35. Li, Z. et al. Graphene quantum dots doping of MoS2 monolayers. *Adv. Mater.* **27**, 5235–5240 (2015).
36. Chaudhary, R., Patel, K., Sinha, R. K., Kumar, S. & Tyagi, P. K. Potential application of mono/bi-layer molybdenum disulfide (MoS2) sheet as an efficient transparent conducting electrode in silicon heterojunction solar cells. *J. Appl. Phys.* **120**, 013104 (2016).
37. Rashid, H. et al. Prospects of molybdenum disulfide (MoS2) as an alternative absorber layer material in thin film solar cells from numerical modeling. *Chalcogenide Lett.* **11**, 397–403 (2014).
38. Rai, A. et al. Progress in contact, doping and mobility engineering of MoS2: an atomically thin 2D semiconductor. *Crystals* **8**, 316 (2018).
39. Suh, J. et al. Doping against the native propensity of MoS2: degenerate hole doping by cation substitution. *Nano Lett.* **14**, 6976–6982 (2014).
40. Rajagopal, A. K. & Callaway, J. Inhomogeneous electron gas. *Phys. Rev. B* **7**, 1912–1919 (1973).
41. Soler, J. M. et al. The SIESTA method for ab initio order-N materials simulation. *J. Phys. Condens. Matter* **14**, 2745–2779 (2002).
42. Perdew, J. P., Burke, K. & Ernzerhof, M. Generalized gradient approximation made simple. *Phys. Rev. Lett.* **77**, 3865–3868 (1996).
43. Goedecker, S., Teter, M. & Hutter, J. Separable dual-space Gaussian pseudopotentials. *Phys. Rev. B* **54**, 1703–1710 (1996).
44. Grimme, S., Antony, J., Ehrlich, S. & Krieg, H. A consistent and accurate ab initio parametrization of density functional dispersion correction (DFT-D) for the 94 elements H-Pu. *J. Chem. Phys.* **132**, 154104 (2010).

ACKNOWLEDGEMENTS

We would like to acknowledge Natural Sciences and Engineering Research Council of Canada award #06096 for funding this work.

AUTHOR CONTRIBUTIONS

J.G. conducted all the simulations. J.G. and M.G. analyzed and wrote the manuscript.

COMPETING INTERESTS

The authors declare no competing interests.

ADDITIONAL INFORMATION

Correspondence and requests for materials should be addressed to M.G.

Reprints and permission information is available at http://www.nature.com/reprints

Publisher's note Springer Nature remains neutral with regard to jurisdictional claims in published maps and institutional affiliations.